

同濟大學

本科生毕业设计（论文）

外文科技文献译文

译文题目	使用观测和气象数据的生成对抗网络 预测台风路径和强度
(外文题目)	Prediction of Typhoon Track and Intensity Using a Generative Adversarial Network With Observational and Meteorological Data
学 院	软件学院
专 业	软件工程
学 号	2051840
学生姓名	梁厚
日 期	2024 年 06 月 12 日

指导教师签名	穆斌	日期	2024.06.13
--------	----	----	------------

使用观测和气象数据的生成对抗网络预测台风路径和强度

摘要：为了挽救生命并减少台风破坏性影响所造成的损失，迫切需要一种准确、快速的预报方法。特别是，短提前期的预测（称为临近预报）依赖于快速预测，可以在受影响地区立即制定应急计划。在本文中，我们提出了在单个图形处理单元上运行的生成对抗网络，以在不到一秒的时间预测台风的路径和强度。为了研究气象变量对台风预报的影响，我们进行了 6 小时路径 预报的参数研究。研究结果表明，学习速度、温度、压力和湿度以及卫星图像对预测准确性有积极影响。为了解决观测数据获取有限的问题并促进 12 小时间隔的预测，我们用总云量和涡度场的再分析数据取代了卫星图像。此次更换导致台风数据由 76 个增加到 757 个，6 小时路径预报误差减少了 23.5%。参数研究的最佳组合产生间隔为 6 小时和 12 小时的航迹预测，相应的平均绝对误差为 44.5 公里和 68.7 公里。通过从生成的速度场中提取信息来预测台风强度，6 小时和 12 小时间隔预报的平均命中率分别为 87.3% 和 83.2%。对于 1994 年以后的台风，将 12 小时间隔的路径和强度与联合台风警报中心和东京区域专业气象中心的预测进行比较。

热带气旋（TC）是人类历史上致命的自然灾害之一。其破坏性影响主要是由于台风中心附近的强风和密集云结构附近的强降雨引起的极端洪水[1]。这些威胁在过去几十年中不断加剧。随着全球变暖的存在，由热带气旋引起的风变得比以前更强、更具破坏性[2]。自 1949 年以来，热带气旋的平移速度在全球范围内下降了 10%，在亚洲下降了 30%到 2016 年[3]。这意味着气旋移动得越慢，落在某一地点的降雨量就越大，因此洪水风险就越高。根据这一趋势，预测 TC 的路径和强度是预防灾害的重点。最近的 TC 预测技术主要使用基于数值模拟的动态模型，并在其他技术中表现出优越的预测性能[4]。TC 预测的成功主要归功于超级计算机的发展[5]。例如，欧洲中期天气预报中心 (ECMWF) 运行两台 Cray XC40 系统，以促进对 1.3 公里网格间距的高分辨率分析。两个 Cray XC40 系统均拥有超过 130000 个内核 [6]。然而，使用基于数值方法的动力模型有一个缺点：进行预测所需的时间过长。

对 TC 进行高分辨率数值分析可能需要数小时，这就是官方气旋预测每隔 6 小时发布一次的原因之一 [7]。更快的预测将允许对热带气旋的发展做出立即反应，例如安全措施或救援任务。为了改进传统的热带气旋预测方法，科学家们考虑使用机器学习（ML）作为热带气旋预测的第二种预测方法。机器学习技术不仅能够捕获非线性模式和复杂关系，而且其计算成本也比数值模拟低得多。因此，许多研究都对通过机器学习预测路径和强度的 TC 预测模型进行了研究[8]-[15]。尽管这些研究极大地提高了预测精度并降低了计算成本，但仍有一些目标必须实现。首先，大多数研究要么预测 TC 的轨迹，要么预测强度，但只有少数研究同时关注这两个属性。热带气旋的路径和强度在天气预报中都很重要，应该同时预测。以往研究的另一个缺点是没有考虑各种气象参数，如速度、海面温度和湿度。据作者所知，还没有使用机器学习方法的研究对各种气象变量对 TC 预测的影响进行了深入分析。为了实现这些目标，本研究开发了一种生成对抗网络（GAN）来预测西北太平洋形成的热带气旋（也称为台风）的路径和强度。在作者之前的研究 [16] 中，GAN 以卫星图像的形式学习按时间顺序排列的观测数据，能够以极小的计算成本很好地预测轨迹。具体来

说，本研究提供了以下三个主要贡献：

- 探讨各种气象资料对台风路径和强度预测的影响，进行系统参数研究，确定卫星影像与气象资料的台风预测最佳组合。

- 探索使用再分析数据来解决卫星图像数量不足的问题。再分析数据在数量和可访问性方面比观测数据具有优势。因此，用总云量（TCC）和涡度场的再分析数据代替卫星图像来克服卫星图像的局限性。因此，台风的数量可以从 76 个增加到 757 个。这种增加使得 GAN 能够学习 1979 年到 2018 年所有台风的大量数据（从形成到消散）。

- 对台风路径和强度进行 6 小时和 12 小时预报，并与联合台风预警中心（JTWC）和国家气象局的预报进行比较。

东京区域专业气象中心（RSMC）。请注意，该研究的目的并不是取代现有的预报技术。天气预报的主要目标是拯救生命和财产。这样一项重要的任务应该由业务预报中心的“一个声音”来执行，使用高度准确的分辨率预测来缩短交付时间，称为临近预报，这对于应急计划很重要[17]。用临近预报技术补充传统方法有助于更快地估计轨迹和强度的突然变化，并更快地制定救生措施。

多尺度 GAN 用于预测台风的路径和强度。该网络学习根据过去的时空特征来预测台风的未来行为。这些特征是从包含物理量的卫星图像和气象数据的观测数据中提取的。下面给出了有关输入数据的选择、深度学习技术以及用于估计预测准确性的指标的详细信息。

卫星图像由韩国气象厅提供[18]，包含 1993 年至 2017 年袭击或即将袭击朝鲜半岛的 76 场台风。由于不同的卫星已经运行了 25 年，因此在将卫星图像用于 GAN 之前，需要有关卫星的详细信息和预处理步骤，类似于 Rüttgers 等人的研究[16]。所有输入卫星图像的大小均为 250×238 个单元格和三个颜色通道 [即 R（红色）、G（绿色）和 B（蓝色）]。每张卫星图像都在台风中心标有红色方块。台风中心的纬度（ ϕ ）和经度（ λ ）坐标由日本气象厅（JMA）提供[19]。为了用红色方块标记每个卫星图像，将 ϕ 和 λ 坐标转换为图像中的笛卡尔坐标。总共存储了 1,628 张图像，图像之间的时间步长为 6 h。案例 1-4 采用观测数据，这些数据包括台风的诞生、发展和死亡。气象数据是从 ECMWF [21] 提供的公共数据集 ERA-interim [20] 中提取的。ERA-interim 是全球大气再分析数据集，于 1979 年启动并不断更新。它使用固定版本的数值天气预报系统（即 IFSCyкφrπ）来生成重新分析的数据。可用数据的时间步长为 6 小时，覆盖了整个地球。网格分辨率为 0.75° 的原始数据通过线性插值细化为 0.125° [22]。对于情况 1-4，仅选择朝鲜半岛周边地区。地图类型的朗伯等角圆锥曲线用于匹配卫星图像的视图。当用重新分析替换观测数据时数据中，空间范围扩展到整个东南亚。对于东经 100-180° 和北纬 0-50° 的空间范围，选择地图类型等距柱状图。对于更具挑战性的 12 小时预测，台风中心坐标信息补充了附加信息独立输入通道。在此通道中，台风中心周围的 3×3 框填充值为 1，数组的其余部分填充遵循正态分布的数字。本研究使用的正态分布如下：

$$f(x) = \frac{1}{\sigma\sqrt{2\pi}} e^{-\frac{(x-x_c)^2+(y-y_c)^2}{2\sigma^2}},$$

式中， x 、 y 分别为经纬度坐标，下标 c 为台风中心坐标。分布的方差 σ^2 设置为

0.04 以匹配其他参数的标准差。因此，矩阵的最大值在中心为 1，矩阵中的所有值都在 0~1 的范围内。高值表明成为台风中心的可能性很高。

在使用训练数据作为 GAN 的输入图像之前，它们被裁剪为总共 5,000,000 个片段，网格大小为 32×32 。如此多的训练片段可以防止过度拟合。此外，使用裁剪部分可以减少一个训练步骤中消耗的内存，并且专注于剪辑的小部分使我们的方法能够有效地学习图像的细节。一个剪辑包含一组来自过去的 m 个连续裁剪的观测和气象数据以及一个地面实况图像。在之前的工作中，我们发现 $m = 4$ 会产生最佳结果 [16]。裁剪后的训练剪辑是使用基于 GAN 的视频建模架构中的深度学习网络的变体进行训练的 [23]。该架构包含一个纯卷积神经网络（即生成器）和一个网络。

将卷积层与池化层和全连接层（即鉴别器）相结合（图 1）。生成器网络获取剪辑，将其单元值标准化为 $(-1; 1)$ ，预测未来情况 (G_0) 的卫星图像和/或气象数据的 32×32 部分，并对预测的单元进行非标准化。GAN 是多尺度网络；因此，生成器网络生成不同尺度 k 的图像 G_k ($G_0 : 32 \times 32, G_1 : 16 \times 16, G_2 : 8 \times 8, G_3 : 4 \times 4$)。生成的网格尺寸为 4×4 、 8×8 和 16×16 的图像可作为下一个更大比例的附加输入。此功能有助于维持长程依赖性并在整个卷积学习过程中保留高分辨率信息。同时，鉴别器网络在每个尺度上对生成的图像和地面真实图像进行分类。后者是从原始全尺寸数据缩小的。输出层提供 0 和 1 之间的二进制输出（即 D_0 、 D_1 、 D_2 、 D_3 ），其中 0 表示生成的图像，1 表示真实情况。生成器模型经过训练以最小化损失函数的组合。

$$L_2^k = \|G_k(I) - \mathcal{G}_k(I)\|_2^2,$$

其中 $\lambda_{l_1} = 1$ ， $\lambda_{gdl} = 1$ ， $\lambda_{adv} = 0.05$ [16]。损失函数 L_k 评估预测图像和提供图像之间的显式差异（2-范数），计算如下：

$$L_2^k = \|G_k(I) - \mathcal{G}_k(I)\|_2^2,$$

其中 I 是输入数据， $G_k(I)$ 是来自提供的地面实况图像的 $12 \times k$ 大小调整后的图像。为了减少模糊，Mathieu 等人。[23]提出了梯度差损失函数（GDL），并报道与其他方法（包括 Ranzato 等人提出的基于循环神经网络的方法）相比，具有 GDL 的 GAN 提高了视频建模性能[41]。GDL， L_{kgdl} ，比较差异预测图像和提供图像的梯度之间如下：

$$L_{gdl}^k = \sum_{i=0}^{n_x-2} \sum_{j=0}^{n_y-2} \left\{ \left| \mathcal{G}_k(I)_{(i+1,j+1)} - \mathcal{G}_k(I)_{(i,j+1)} \right| \right. \\ \left. - \left| G_k(I)_{(i+1,j+1)} - G_k(I)_{(i,j+1)} \right| \right| \\ \left. + \left| \mathcal{G}_k(I)_{(i+1,j+1)} - \mathcal{G}_k(I)_{(i+1,j)} \right| \right. \\ \left. - \left| G_k(I)_{(i+1,j+1)} - G_k(I)_{(i+1,j)} \right| \right\},$$

其中 n_x 和 n_y 是图像的宽度和高度的像素数, (i, j) 是像素坐标。 $L_{G,kadv}$ 损失函数用于支持生成器模型, 通过生成与提供的地面真实图像无法区分的图像来欺骗鉴别器网络, 如下所示:

$$L_{adv}^{G,k} = L_{bce}(D_k(G_k(I)), 1),$$

其中 L_{bce} 是二元交叉熵损失函数, 定义为:

$$L_{bce}(a, b) = -b \log(a) - (1 - b) \log(1 - a),$$

对于介于 0 和 1 之间的标量 a 和 b 。鉴别器模型经过训练, 可将损失函数最小化为

$$L_{discriminator} = \frac{1}{4} \sum_{k=0}^3 [L_{bce}(D_k(\mathcal{G}_k(I)), 1) \\ + L_{bce}(D_k(G_k(I)), 0)].$$

当生成的数据和地面真实数据被正确区分时, 鉴别器损失最小化, 而随着鉴别器被生成的图像成功欺骗, 生成器损失减少。测试步骤使用未裁剪的全尺寸测试数据进行。选择 32×32 的网格大小是为了有效利用图形处理单元 (GPU) 内存。尽管生成器网络是使用小片段进行训练的, 但由于其卷积性质, 它最终会学习到具有较大片段的网络所学习到的相同权重。在测试期间, 预测具有大 (250×238) 块的台风卫星图像。由于生成器的完全卷积架构, 这再次成为可能。

GAN 是从头开始训练的。生成器网络的权重和偏差由自适应矩 (ADAM) 优化器 [42] 以 0.04 的学习率进行更新。鉴别器以 0.02 的学习率与随机梯度去优化器一起运行。表 1 提供了生成器和鉴别器网络的详细配置。输入通道的数量 (N_i) 可以变化, 以确保网络考虑输入数据的不同组合。当 GAN 仅使用卫星图像时, 需要三个通道。如果加上其他气象数据, 通道数量就会增加。

预测精度是借助绝对误差 (E) 来估计的。E 的计算单位为公里 (km), 通过应用超正弦公式[26], 其中地球半径 R 取自每个序列的真实地面坐标位置:

其中 ϕ 和 λ 分别是纬度和经度坐标。下标 $pred$ 和 $real$ 分别表示当前 GAN 预测的坐标变量和地面真值坐标变量。显着图用于可视化每个参数如何影响结果。图像 I 的得分函

数 $S(I)$ 由以下方程定义。其中 w 和 b 分别是模型的权重向量和偏差。显著性图被归一化 $\text{yield-ing } \{\hat{S}(I) \in \mathbb{R} | 0 \leq \hat{S}(I) \leq 1\}$, 值越接近 1, 参数对预测的贡献越大。Simonyan 等人的论文解释了该技术的详细信息[27]。研究了气象输入数据不同组合的四种情况, 以确定气象变量对台风预测的影响。GAN 在 NVIDIA Tesla K90 GPU 上接受了 72 小时的训练。表 2 总结了考虑的输入参数组合。最初, 该研究尝试对 10 个测试台风进行 6 小时预测, 而 GAN 尚未接受过训练。预测与一个称为序列的数字相关联。Onesequence 代表 $m \times N$ 按时间顺序排列的输入图像, 这些图像被馈送到 GAN、地面实况数据和网络生成的预测图像。在本研究的框架中, 参数研究中应用 $m = 4$ 作为最佳选项 [16]。这种情况意味着 GAN 接收了过去 24 小时 (4×6 小时) 的信息。

我们之前的研究 [16] 展示了将表面速度数据添加到卫星图像中作为 GAN 的输入如何减少台风中心预测的平均误差、如何最小化误差波动以及如何提高预测云图像的质量。然而, 先前研究的一个关键缺点是预测的可靠性。在 165 个测试序列中的 5 个中, GAN 未能成功生成台风中心。这个结果是不可接受的, 因为台风追踪中的停电可能会造成致命的后果。因此, 后续章节将研究利用观测和气象数据实现准确且可靠的台风预报的方法。

在案例 1 中, 压力水平为 200、850 和 950 mb 的速度场被添加到我们之前研究 [16] 的输入中, 包括卫星图像和 10 m 高度的速度场。由于各种原因选择这些压力水平。台风的特点是不同横向位置和高度度的最大速度不同。台风眼壁是围绕风眼的一个环是最关键的区域。GPS 落风探空仪的测量表明, 飓风在 500 m 高度左右具有最强的平均眼墙风速 [28]。ERA-interim 数据集的气压水平中, 950 mb 的气压水平最接近 500 m 的海拔高度。在分析环境风切变及其对台风的影响时, 通常使用 850 和 200 mb 气压水平的海拔高度[29]。在台风中, 风切变影响潮湿空气通过柱体从地表上升到高海拔地区, 在高海拔地区由于凝结而释放出潜热。潜热为台风提供能量。低垂直风切变增强了该柱以及内部的吸力效果, 因为该柱的下部和上部部分是对齐的。同时, 高垂直风切变使立柱难以保持所有部件对齐并产生强大的吸力效应。因此, 案例 1 的输入包括卫星图像、表面速度以及 200、850 和 950 mb 压力水平下的速度由于只有一场台风, 案例 1 的预测比之前的研究 [16] 显示出更高的可靠性。GAN 未识别中心 (台风马拉卡斯的序列 21)。在案例 1 中, 当台风 Neoguri 接近韩国和日本大陆时, GAN 对序列 15 产生了明显较高的误差 (图 2)。该峰值导致台风 Neoguri 的平均误差和标准偏差被放大 (图 3)。在台风紫罗兰和梅美的图像中, 旋转运动没有清晰地再现 (图 4a 和 c)。对 TC Maemi 的序列 15 (图 5) 进行了分析, 这是一个具有挑战性的序列, 在登陆附近有分散的台风。速度分量的显著图的特点是总体得分较高 (0.336), 主要发生在靠近台风的区域。台风结构 (图 5a) 表明, 这些区域附近的瞬时速度对路径预测起着重要作用, 但随着距台风中心距离的增加, 其影响逐渐减弱。

在案例 2 中, 卫星图像与表面压力数据相结合, 但没有速度数据。观测到多个误差峰, 如台风"奥利瓦"序列 11、台风"前美"序列 13、台风"兔"序列 13、台风"梅法"序列 6、台风"尼古里"登陆前的几个序列 (图 2)。尚未确定一个台风中心 (台风"拉玛孙"的序列 16)。从总体上看, 案例 2 和案例 1 的可靠性水平相似, 但案例 2 的平均误差比案例 1 增加了 40.8% (图 3)。案例 2 的平均误差幅度是所有测试台风 (马拉喀斯除外) 的所有案例中最高的。同时, 几乎所有测试的台风中, 情况 2 的误差波动都远高于情况 1 (图 3)。具体而言, 观察到台风"紫罗兰"、"奥利瓦"、"前美"、"阿兔"、"穆法"和"尼古里"的不确定性显著增加。案例 2 生成的图像与 Rüttgers 等人的研究中的图像类似。[16] (图 4)。云看起来是静态的, 云结构的旋转运动无法被清楚地识别。在案例 3 中, 案例 1 的数据与表面压力场

相结合。案例 1 和案例 3 的结果比较表明，与案例 1 相比，增加表面压力使所有序列的平均误差降低了 3.4%（图 3）。在台风 Saomai 的序列 9 和序列 13-15 中观察到了稳定效果的示例。台风阿兔向北偏转。然而，对于这两种情况，接近登陆时的预测都具有挑战性（图 2）。对于几种台风（即紫罗兰、奥利瓦和梅美），情况 1 显示了台风接近大陆时的困难。对于其他台风（即"拉玛太阳"、"天兔"、"穆法"和"马拉卡斯"），案例 3 的结果显示在同一情况下存在较高的误差。这两起案件都与台风"新古里"的登陆有关。GAN 未能可靠地预测台风紫罗兰序列 10 的中心。总体而言，案例 3 的云图与案例 1 相似（图 4）。然而，台风紫罗兰的旋转（图 4a）和台风中心下方的消散云结构。Maemi（图 4c）的预测与地面实况图像的相似度有所提高。与速度场的显着图（0.336）相比，表面压力的显着图（图 5b）的平均得分较低（0.129）（图 5a）。这强调了瞬时速度信息对于对流主导的短期轨迹预测物理学的重要性。然而，我们在压力图中可以看到的有趣的方面是，整个域的全球压力分布正在影响台风的路径。

速度场和表面压力的分布提供了有关台风当前状态的信息。然而，运动和强度取决于影响台风的时滞物理量。海面温度（SST）就是这样一个量。一般来说，海面温暖的海水保证了高蒸发率、空气中的高含水量以及台风所需的足够能量[30]。强对流通常需要约 26.5°C 的海温阈值，以确保足够的潮湿空气上升，并形成热带台风[31]。当温度低于 26.5°C 时，浮力不够强，下沉克服了对流。同时，当海温高于 29.0°C 时，对流活动趋于饱和[32]。然而，这仅描述了海温与台风在大气中如何发展之间的相互作用。此外，还应考虑海洋对海温的响应。台风沿气旋（逆时针）方向旋转。它们的旋转运动与海洋表层耦合。台风的规模足够大，足以受到旋转地球的科里奥利力的影响[33]。这种力导致北半球向右偏转 90° 。因此，表层也发生偏转，这种现象称为埃克曼输运，它会导致海洋表面上涌，从而从深海吸走冷水[34]。第一个原因是台风移动到哪里，哪里就会留下冷水。第二个原因是海洋表面风摩擦引起的海洋上层垂直混合。在表面，破碎波注入气泡并产生高能湍流，导致与深层较冷的水进行交换[35]。海温-大气关系和海温-海洋响应可以用台风"Maemi"的例子来详细说明。图 6a 和 b 显示了一系列台风 Maemi 的卫星图像和相应的压力场。如图所示。

图 6c，在前美移动方向上，靠近韩国和日本海岸，当台风从当前位置向北移动时，温暖的海面增强了台风的强度[36]。这种现象导致了靠近海岸的台风灾难性的强度[37]。由于台风当前位置的海表温度低于其周围的海表温度，冷却效果是显而易见的。另一个对台风产生时滞影响的物理量是相对湿度（RH）。一旦空气上升并且冷凝水释放出大量潜热，潮湿的环境就会与大风暴相关。此外，大量的凝结水与高层的分流空气结合导致外雨带降水，这种现象导致台风风场横向扩展[38]。同时，干燥的空气限制了台风的加强。RH 是气液混合物平衡时水蒸气压与饱和蒸气压的比值。百分比值显示当前水汽负荷与最大水汽负荷的比率。台风"美美"的例子清楚地表明了台风在登陆大陆的过程中如何不断地吸收潮湿空气，这是台风强度高的另一个原因（图 6d）。在案例 4 中，案例 3 的数据与 SST 场和 RH 场合并在 200、850 和 950 mb 的压力水平下。这是最可靠的情况，因为 GAN 没有遗漏任何预测，并且是唯一准确预测两个最具挑战性台风：Usagi 和 Neoguri 中心的情况（图 2）。与其他情况不同，在这种情况下，在其余测试的台风中没有发现高误差峰值。除台风"紫罗兰"和"梅美"外，在案例 3 中添加海温和相对湿度数据可以减少平均误差和误差波动（图 3）。事实上，在这种情况下，总平均误差降低了 12.9%。然而，案例 4 中生成的图像具有与案例 3 类似的云结构（图 4）。然而，预测看起来更可靠，因为在所有生成的图像中预测中心

的颜色强度更清晰。海温和相对湿度对台风路径的预测有很大影响，特别是当台风接近登陆并改变方向时。误差大多在台风接近陆地或之后减少。海表温度和相对湿度层的显著性图强调了这一点（图 5c）。尽管总体得分 (0.142) 与压力图 (0.129) 处于相似的范围，但局部得分并未广泛分布在整个域中。相反，尽管登陆造成风暴强烈分散，但分数还是集中在台风的影响区域。这表明海温和相对湿度对于描述台风登陆期间和登陆后的行为非常有帮助。因此，考虑到精度的提高以及 SST 和 RH 对登陆的影响，情况 4 的组合被认为是最佳选择。

12 小时间隔内的应用范围将更广泛，以补充已建立的轨迹和强度预测方法，以更快地估计突然变化。这种预测的主要限制是台风数据的数量。对于 12 小时间隔内的预测，将相同数量的输入 ($m = 4$) 馈送到 GAN 进行训练。然而，theGAN 预测两个未来时间步的信息：6 小时和 12 小时预测。对于这种情况，案例 1-4 中用于训练 GAN 的台风序列数量不足以执行超过 6 小时的预测。韩国气象局机构[18]只允许我们访问 1993 年至 2017 年袭击或即将袭击朝鲜半岛的 76 个台风的卫星图像，其中 66 个用于训练，10 个用于测试 GAN。为了克服这一限制，卫星图像被重新分析所取代总云量 (TCC) 数据。TCC 通过整合从大气顶部到地表的整个云层来实现 0 到 1 之间的云分数。使用 TCC 数据的一个缺点是旋转与卫星图像中的云形状相比，台风的结构无法清晰识别。因此，压力水平为 200、850 和 950 mb 的涡度场被添加到 TCC 数据中，以提供有关云旋转运动的信息。使用再分析数据而不是卫星图像导致数据从 76 个台风增加到 757 个台风。对于 20 个测试用例，6 小时间隔内的总平均误差降低了 23.5%，达到 44.5 公里（表 3）。

对于案例 4，台风中心的红色标记是可见的。然而，12 小时的时间间隔对新的研究是一个挑战。真实网络和预测 TCC 区域中的红色标记经常变得不清楚或消失。为了改进预测，包含附加信息的输入通道。

添加了关于台风中心坐标的信息，如第 2 节中所述。II-B. ϕ π 小时预报中使用了 737 个台风的训练数据和 20 个台风的测试数据。在 10 多个序列中选取最大风速至少 64 节的 20 个测试案例，表明台风持续时间超过 60 小时。香港天文台分类的九个风速至少为 100 节的超强台风也包括在内。更强的台风更难以预测，因此选择台风来测试极端条件下的网络性能。6 小时和 12 小时预报结果的平均误差分别为 44.5 公里和 68.7 公里（表 3）。对于这两个时间间隔，与没有超强台风的预测相比，仅考虑超强台风的平均误差分别增加了 7.9% 和 13.6%。表 3 列出了测试台风在每个时间间隔的详细结果。误差主要发生在 120-140E 和 30-50N 之间的台风。该地区受反信风影响强烈，台风经常改变方向并加速北上或加速。向东[40]。随着时间间隔的增加，逆信风附近的台风运动误差显著增加。例如，分析了台风 "Faye" ζ 小时和 12 小时间隔的预测轨迹，如图 7 所示。对于 6 小时间隔，预测中心与地面真实情况一致，略有误差。对于 12 小时的间隔，神经网络在捕捉突然偏转后的台风运动方面表现出困难。对于 1994 年以后的台风，JTWC 和 RSMC Tokyo 提供了预报数据。表 3 显示了与 GAN 预测的比较。由于每个业务中心并不提供 1994 年之后所有台风的数据，因此 GAN 的预测部分与 JTWC 的预测进行比较，部分与 RSMC 东京的预测进行比较。为了计算 12 小时比较的平均误差，仅包括 JTWC 和 RSMC 东京预测的台风。神经网络的精度（66.5 公里）与预报中心相比有 21.6% 的优势（84.8 公里）。这种趋势是在没有预测的情况下观察到的超级台风，以及仅包含超级台风的预测。请注意，在本方法中，使用单个 GPU 可以在不到一秒的时间内预测台风和云分布的轨迹。

台风强度按最大持续风速 (MSW) 进行分类，即过去 10 分钟平均表面风速[39]。级别

如下：热带低气压（MSW 33 节或以下）、热带风暴（MSW 34 至 47 节）、强热带风暴（MSW 48 至 63 节）和台风（MSW 64 节或以上）。根据香港天文台的官方分类，增加了 MSW 为 100 节或以上的更强级别（超级台风）。香港天文台也使用 10 分钟的平均周期进行强度分类。为了预测台风强度，仅考虑案例 4 的配置。MSW 是从 10 m 高度处的预测速度场得出的，然后分配给相应的强度等级。输入数据、输出数据和损失函数与轨迹预测相匹配。最大风速出现在距台风中心 500 公里半径范围内。6 h 和 12 h 时间间隔提取的台风强度命中率分别为 87.3% 和 83.2%（表 3）。同时，超强台风 12 小时预报的平均命中率比其余台风的命中率低 3.9%，6 小时预报的平均命中率高 2.3%。表 3 列出了测试的台风在每个时间间隔的详细结果。如图 8 所示，目前的神经网络在预测 25 至 35 N 之间登陆前 60 节以上的强强度时遇到了困难。这可以通过瞬时风的事实来解释。预测过程中数据的消耗和误差随着预测的进行而累积。1994 年以后的台风与预测中心的数据的比较包括用于 12 小时路径预测比较的相同台风。同样，一些强度预测是由 JTWC 提供的，以及 RSMC 东京的其他人。为了计算 12 小时比较的平均误差，仅包括 JTWC 或 RSMC Tokyo 预报的那些台风。GAN 的强度预测对所有台风的平均命中率为 81.3%，而预测中心的平均命中率为 86.4%（表 3）。在排除超强台风的情况下，平均命中率也出现了类似的趋势。请注意，JTWC 对 1 分钟内的地面风进行平均以对台风强度进行分类。

本方法展示了使用单个 GPU 在几秒钟内预测台风路径和强度的“临近预报能力”。尽管基于机器学习的方法与基于数值模拟的台风预测方法有本质上的不同，但它们具有重要的特征，特别是对气象变量的依赖性。请注意，所提出的方法并不旨在取代传统的预测技术。相反，它显示出补充现有技术的巨大潜力预测技术可以产生更快的预测。当台风突然发生变化时，所提出的方法可以节省启动重要安全措施的时间。通过将大量观测数据与更高分辨率的再分析数据相结合以及更长的预测间隔，预计本方法将得到进一步增强。

在这项研究中，我们开发了一种基于 GAN 的临近预报方法，可以预测台风长达 12 小时的路径和强度。人们对气象和观测输入数据的各种组合进行了研究，以确定哪些物理参数有利于预测的可靠性。利用不同高度（200、850 和 950 mb）的速度场、不同高度（200、850 和 950 mb）的表面压力、海面温度和相对湿度、总云量和涡度场在不同海拔高度（200、850 和 950 mb）可实现最佳性能。以此组合对台风路径和强度进行了 6 小时和 12 小时的预测。在台风路径预测中，6 小时和 12 小时预测的平均误差分别为 44.5 和 68.7 km。误差大多发生在 120 - 140 E 和 30 - 50 N 之间，此时台风改变方向并加速。对于 12 小时的间隔，业务预报中心对 1994 年之后的台风进行了预报，并与 GAN 的预报进行了比较。该神经网络对台风中心的预测平均误差为 66.5 km，比现有台风预报系统的 84.8 km 的测试台风准确率更高。6 和 12 间隔预测的命中率分别为 87.3% 和 83.2% 的台风强度。目前基于 GAN 的神经网络系统在预测超过 60 节的高风速方面存在困难，特别是在 25 到 35 N 之间的登陆之前。这可以通过预测过程中发生的瞬时风数据的消散以及预测过程中累积的误差来解释。1994 年以后，GAN（81.3%）和业务预报中心（86.4%）对台风强度的预测只有 5.1% 的微小差异。

Received March 31, 2022, accepted April 21, 2022, date of publication May 3, 2022, date of current version May 10, 2022.

Digital Object Identifier 10.1109/ACCESS.2022.3172301

Prediction of Typhoon Track and Intensity Using a Generative Adversarial Network With Observational and Meteorological Data

MARIO RÜTTGERS^{1,2,3}, SOOHWAN JEON⁴, SANGSEUNG LEE⁵, AND DONGHYUN YOU⁴

¹Institute of Aerodynamics and Chair of Fluid Mechanics (AIA), RWTH Aachen University, 52062 Aachen, Germany

²Jülich Supercomputing Centre (JSC), Forschungszentrum Jülich GmbH, 52425 Jülich, Germany

³Jülich Aachen Research Alliance - Center for Simulation and Data Science (JARA-CSD), 52074 Aachen, Germany

⁴Department of Mechanical Engineering, Pohang University of Science and Technology (POSTECH), Pohang 37673, Republic of Korea

⁵Department of Mechanical Engineering, Inha University, Incheon 22212, Republic of Korea

Corresponding author: Donghyun You (dhyou@postech.ac.kr)

This work was supported in part by the Samsung Research Funding Center of Samsung Electronics under Project SRFC-TB1703-51, and in part by the National Research Foundation of Korea (NRF) under Grant NRF-2019K1A3A1A74107685 and Grant NRF-2021R1A2C2092146.

ABSTRACT To save lives and reduce damage from the destructive impacts of a typhoon, an accurate and fast forecast method is highly demanded. Particularly, predictions for short lead times, known as nowcasting, rely on fast forecasts allowing immediate emergency plannings in the affected areas. In this paper, we propose a generative adversarial network that operates on a single graphics processing unit, to predict both the track and intensity of typhoons for short lead times within fractions of a second. To investigate the effects of meteorological variables on typhoon forecasts, we conducted a parameter study for 6-h track predictions. The results of the study indicate that learning velocity, temperature, pressure, and humidity along with satellite images have positive effects on prediction accuracy. To address the limited access to observational data and facilitate predictions for 12-h intervals, we replaced satellite images with reanalysis data of the total cloud cover and vorticity fields. This replacement led to an increase in data from 76 to 757 typhoons, and it reduced the error of the 6-h track forecasts by 23.5%. The best combination of the parameter study yields track predictions in intervals of 6 and 12 h with the corresponding averaged absolute errors of 44.5 and 68.7 km. Typhoon intensities are predicted by extracting information from generated velocity fields with averaged hit rates of 87.3% and 83.2% for 6- and 12-h interval forecasts, respectively. For typhoons after 1994, tracks and intensities for 12-h intervals are compared to forecasts from the Joint Typhoon Warning Center and Regional Specialized Meteorological Center Tokyo.

INDEX TERMS Typhoon track prediction, typhoon intensity prediction, deep learning, nowcasting.

I. INTRODUCTION

Tropical cyclones (TCs) are among the fatal natural disasters in human history. Their destructive impacts are mainly due to strong winds near the center of a typhoon and extreme flooding caused by heavy rainfall near dense cloud structures [1]. These threats have intensified over the past decades. Winds due to TCs are becoming stronger and more destructive than before with the existence of global warming [2]. Translation speeds of TCs have decreased by 10% globally and by 30% in Asia from 1949 to 2016 [3]. This implies that

the slower a cyclone moves, the larger the amount of rain that falls on one location, and thus the higher the flooding risk. Based on this trend, the focus should be on predicting the path and intensity of TCs to prevent disasters. Recent prediction techniques on TCs mainly use a dynamic model based on a numerical simulation and exhibit superior prediction performance among other techniques [4]. The success in TC prediction was mainly due to the development of supercomputers [5]. For example, the European Centre for Medium-Range Weather Forecasts (ECMWF) operates two Cray XC40 systems to facilitate a high-resolution analysis of the grid spacing of 1.3 km. Each of the two Cray XC40 systems has over 130,000 cores [6]. However, one drawback

The associate editor coordinating the review of this manuscript and approving it for publication was Lefei Zhang¹.

of using dynamical models based on numerical methods is the time required to make forecasts. A high-resolution numerical analysis of TCs can take hours, and this is one reason why official cyclone predictions are released in a 6-h time interval [7]. Faster predictions would allow immediate reactions to the development of a TC, such as safety measures or rescue missions.

To improve traditional TC prediction methods, scientists have considered using machine learning (ML) as a second predictive method for TC predictions. ML techniques are not only able to capture non-linear patterns and complex relationships, but their computational costs are also much lower than those of numerical simulations. Therefore, TC forecast modeling to predict the track and intensity through ML has been investigated in many studies [8]–[15]. Although these studies have improved the prediction accuracy and reduced the computational cost drastically, some objectives must be achieved. First, in most studies, either the track or the intensity of TCs is predicted, but only a few studies focus on both properties. As the track and intensity of a TC are both important in weather forecasts, they should be predicted simultaneously. Another shortcoming of the previous studies is that they did not consider various meteorological parameters, such as velocities, sea surface temperature, and humidity. To the best of the authors' knowledge, no studies that use ML methods have conducted an in-depth analysis of how TC predictions are influenced by various meteorological variables.

To achieve these goals, the present study develops a generative adversarial network (GAN) to predict both the track and intensity of a TC that forms in the north-western Pacific Ocean, also known as a typhoon. In the authors' previous study [16], a GAN that learns chronologically ordered observational data in the form of satellite images was able to predict the tracks reasonably well with miniscule computational cost.

Specifically, the present study provides the following three major contributions:

- To investigate the effects of various meteorological data in the prediction of the typhoon track and intensity, a systematic parameter study is conducted, and the best combination of satellite images and meteorological data for typhoon predictions is determined.
- Using reanalysis data to address the insufficient number of satellite images is explored. Reanalysis data have advantages over observational data in terms of quantity and accessibility. Thus, the replacement of satellite images with reanalysis data of the total cloud cover (TCC) and vorticity fields is performed to overcome the limited satellite images. Consequently, the number of typhoons can be increased from 76 to 757. This increase allows the GAN to learn a large amount of data (from formation to dissipation) of all typhoons from 1979 to 2018.
- 6- and 12-h forecasts of the track and intensity of a typhoon are conducted and compared with forecasts from the Joint Typhoon Warning Center (JTWC) and the

Regional Specialized Meteorological Center (RSMC) Tokyo.

Note that the study does not aim to replace established forecasting techniques. The main objective of weather forecasting is to save lives and properties. Such an important task should be performed by “one voice” from operational forecasting centers using highly accurate resolution predictions for short lead times, known as nowcasting, which is important for emergency planning [17]. Complementing conventional methods with nowcasting techniques helps obtain faster estimates of sudden changes in the track and intensity and formulate life-saving measures quicker.

II. METHODOLOGY

A multi-scale GAN is used to predict tracks and intensities of typhoons. The network learns to predict the future behavior of a typhoon based on spatio-temporal features from the past. These features are extracted from observational data in form of satellite images and meteorological data that contain physical quantities. Details about the selection of input data, the deep learning technique, and metrics used to estimate the accuracy of predictions are given below.

A. OBSERVATIONAL DATA

Satellite images are provided by the Korean Meteorological Agency [18] and contain 76 typhoons from 1993 to 2017 that hit or were about to hit the Korean peninsula. Because different satellites have been operating in the 25-year period, detailed information about the satellites and pre-processing steps are necessary before using satellite images for the GAN, similar to the study of Rüttgers *et al.* [16]. All input satellite images have a size of 250×238 cells and three color channels [i.e., R (red), G (green), and B (blue)]. Each satellite image is labeled with a red square at a typhoon center. The latitudinal (ϕ) and longitudinal (λ) coordinates of typhoon centers are provided by the Japan Meteorological Agency (JMA) [19]. To label each satellite image with a red square, the ϕ and λ coordinates are transferred to Cartesian coordinates in the image. A total of 1,628 images are stored, with a time step size of 6 h between images. Observational data are used in Cases 1–4, and these data included birth, development, and death of typhoons.

B. METEOROLOGICAL DATA

Meteorological data are extracted from the public dataset ERA-interim [20] provided by ECMWF [21]. The ERA-interim is a global atmospheric reanalysis dataset, which was started in 1979 and is continuously updated. It uses a fixed version of a numerical weather prediction system (i.e., IFS-Cy31r2) to produce reanalyzed data. The available data have a time step of 6 h and cover the entire globe. Raw data with grid resolution of 0.75° are refined to 0.125° through linear interpolation [22]. For Cases 1–4, only the area around the Korean peninsula is selected. The map-type Lambert conformal conic is used to match the view of satellite images. When replacing observational data with reanalysis

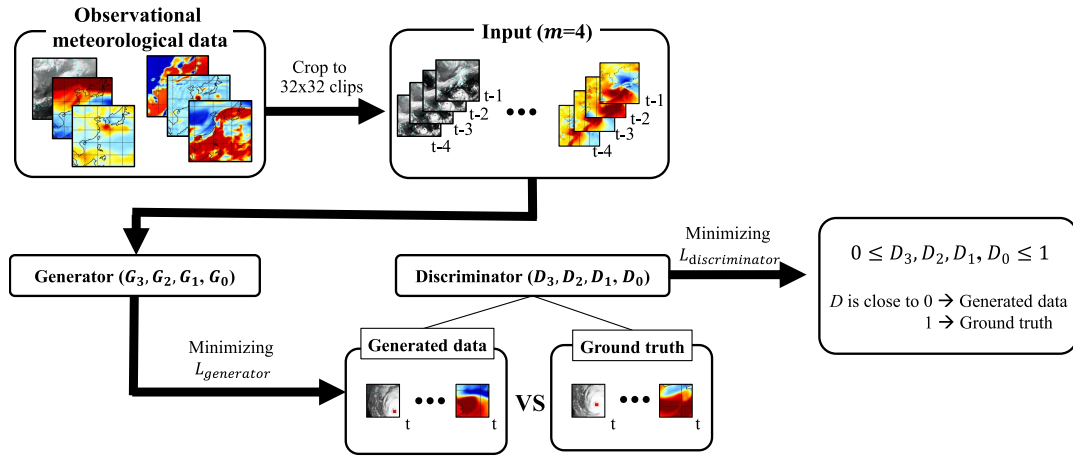


FIGURE 1. Architecture of the utilized GAN.

data, the spatial range is extended to entire Southeast Asia. The map-type equirectangular is selected for spatial ranges of 100–180 E and 0–50 N.

For the more challenging 12-hour predictions, information on typhoon center coordinates is complemented with an additional input channel. In this channel, a 3×3 box around the center of the typhoon is filled with the value of 1, and the rest of the array is filled with numbers following a normal distribution. The normal distribution used in this study is as follows:

$$f(x) = \frac{1}{\sigma\sqrt{2\pi}} e^{\frac{(x-x_c)^2 + (y-y_c)^2}{-2\sigma^2}}, \quad (1)$$

where x and y are longitudinal and latitudinal coordinates, respectively, and the subscript c indicates the coordinates of the typhoon center. The variance of the distribution σ^2 is set to 0.04 to match the standard deviation of the other parameters. Therefore, the maximum value of the matrix is unity at the center, and all the values in the matrix are in the range of 0–1. High values indicate a high possibility of being the typhoon center.

C. DEEP LEARNING TECHNIQUE

Prior to using the training data as input images to the GAN, they are cropped to a total number of 5,000,000 clips with a grid size of 32×32 . Such numerous training clips prevent overfitting. Furthermore, using cropped parts reduces the memory consumed in one training step and focusing on small parts of a clip allows our method to effectively learn the details of an image. A clip contains a set of m consecutively cropped observational and meteorological data from the past and one ground truth image. In the previous work, we found that $m = 4$ produces the best results [16].

The cropped training clips are trained using variations of deep learning networks in a GAN-based video modeling architecture [23]. This architecture contains a pure convolutional neural network (i.e., the generator) and a network that

combines convolutional layers with pooling and fully connected layers (i.e., the discriminator) (Fig. 1). The generator network takes a clip, normalizes its cell values to $(-1; 1)$, predicts a 32×32 part of satellite images and/or meteorological data for a future occasion (G_0), and denormalizes the predicted cells. GANs are multi-scale networks; thus, the generator network generates images G_k of different scales k (G_0 : 32×32 , G_1 : 16×16 , G_2 : 8×8 , G_3 : 4×4). Generated images with grid sizes of 4×4 , 8×8 , and 16×16 function as additional inputs for the next larger scale. This feature helps maintain long-range dependencies and preserves high-resolution information throughout the convolutional learning. Meanwhile, the discriminator network classifies the generated and ground truth images at each scale. The latter are downsampled from the original full scale data. The output layer provides binary outputs (i.e., D_0, D_1, D_2, D_3) between 0 and 1, where 0 denotes the generated image and 1 represents the ground truth.

The generator model is trained to minimize the combination of loss functions

$$L_{generator} = 1/4 \sum_{k=0}^3 \lambda_{l2} L_2^k + \lambda_{gdl} L_{gdl}^k + \lambda_{adv} L_{adv}^{G,k}, \quad (2)$$

where $\lambda_{l2} = 1$, $\lambda_{gdl} = 1$, and $\lambda_{adv} = 0.05$ [16]. The loss function L_2^k evaluates the explicit difference (2-norm) between the predicted and provided images and is computed as follows:

$$L_2^k = ||G_k(I) - \mathcal{G}_k(I)||_2^2, \quad (3)$$

with I being the input data and $\mathcal{G}_k(I)$ being a $\frac{1}{2^k}$ resized image from the provided ground truth image. To reduce blurriness, Mathieu et al. [23] proposed a gradient difference loss function (GDL) and reported that the GAN with GDL improves the video modeling performance compared to other methods including a recurrent neural network based method proposed by Ranzato et al [41]. The GDL, L_{gdl}^k , compares the difference

TABLE 1. The detailed configuration of the generator and discriminator networks. N_i indicates the number of channels of the input data.

Generator model				
Convolutional layers	G_3	G_2	G_1	G_0
Feature map numbers	$N_i m$ 64 128 64 N_i	$N_i(m+1)$ 64 128 64 N_i	$N_i(m+1)$ 64 128 256 128 64 N_i	$N_i(m+1)$ 64 128 256 128 64 N_i
Discriminator model				
Convolutional layers	D_3	D_2	D_1	D_0
Feature map numbers	N_i 32	N_i 32 64 64	N_i 64 128 128	N_i 64 128 256 64
Fully connected layers				
Neuron numbers	512 256 1	1024 512 1	1024 512 1	1024 512 1

between gradients of the predicted and provided images as follows:

$$L_{gdl}^k = \sum_{i=0}^{n_x-2} \sum_{j=0}^{n_y-2} \left\{ \left| \mathcal{G}_k(I)_{(i+1,j+1)} - \mathcal{G}_k(I)_{(i,j+1)} \right| \right. \\ \left. - \left| G_k(I)_{(i+1,j+1)} - G_k(I)_{(i,j+1)} \right| \right. \\ \left. + \left| \mathcal{G}_k(I)_{(i+1,j+1)} - \mathcal{G}_k(I)_{(i+1,j)} \right| \right. \\ \left. - \left| G_k(I)_{(i+1,j+1)} - G_k(I)_{(i+1,j)} \right| \right\}, \quad (4)$$

where n_x and n_y are numbers of pixel in the width and the height of an image, and (i, j) is a pixel coordinate. The $L_{adv}^{G,k}$ loss function is employed to support the generator model to delude the discriminator network by generating images which are indistinguishable from the provided ground truth images as follows:

$$L_{adv}^{G,k} = L_{bce}(D_k(G_k(I)), 1), \quad (5)$$

where L_{bce} is the binary cross entropy loss function defined as

$$L_{bce}(a, b) = -b \log(a) - (1 - b) \log(1 - a), \quad (6)$$

for scalars a and b between 0 and 1.

The discriminator model is trained to minimize a loss function as

$$L_{discriminator} = \frac{1}{4} \sum_{k=0}^3 [L_{bce}(D_k(\mathcal{G}_k(I)), 1) \\ + L_{bce}(D_k(G_k(I)), 0)]. \quad (7)$$

The discriminator loss is minimized, as the generated and the ground truth data are distinguished correctly, while the generator loss decreases as the discriminator is successfully deluded by the generated images. Testing steps are performed with full-scale test data without being cropped.

The grid size of 32×32 is selected for the efficient usage of the graphics processing unit (GPU) memory. Although the generator network is trained with small clips, due to its convolutional nature, it eventually learns the same weights learned by a network with larger clips. During tests, typhoon satellite images with large (250×238) patches are predicted. This is again possible because of the fully convolutional architecture of the generator.

The GAN is trained from scratch. The weights and biases of the generator network are updated by an adaptive moments (ADAM) optimizer [42] at a learning rate of 0.04. The discriminator operates with a stochastic gradient decent optimizer at a learning rate of 0.02. The detailed configuration of the generator and discriminator networks is provided in Table 1. The number of input channels (N_i) can be varied to ensure that the network considers different combinations of input data. Three channels are required when the GAN uses satellite images only. If other meteorological data are added, the number of channels increases.

D. ERRORS IN THE PREDICTION OF TYPHOON CENTERS

Prediction accuracy is estimated with the help of the absolute error (E). E is calculated in kilometers (km) by applying the hypersine formula [26] with Earth radius R taken at the location of the real coordinates of the ground truth of each sequence:

$$E = 2R \arcsin \left(\sin^2 \left(\frac{\phi_{pred} - \phi_{real}}{2} \right) \right. \\ \left. + \cos \phi_{real} \cos \phi_{pred} \sin^2 \left(\frac{\lambda_{pred} - \lambda_{real}}{2} \right) \right)^{\frac{1}{2}}, \quad (8)$$

where ϕ and λ are latitudinal and longitudinal coordinates, respectively. The subscripts *pred* and *real* indicate coordinate variables predicted by the present GAN and the ground truth coordinate variables, respectively

A saliency map is used to visualize how each parameter influences the results. The score function $S(I)$ for an image I is defined by the following equations:

$$S(I) \approx w^T I + b, \quad (9)$$

$$w = \frac{\partial S}{\partial I}, \quad (10)$$

where w and b are the weight vector and the bias of the model, respectively. The saliency maps are normalized yielding $\{\hat{S}(I) \in \mathbb{R} \mid 0 \leq \hat{S}(I) \leq 1\}$, and the closer the value to 1, the greater the contribution of the parameter to the prediction. Details on this technique are explained in the paper of Simonyan *et al.* [27].

III. EFFECTS OF METEOROLOGICAL DATA ON THE TYPHOON TRACK PREDICTION

Four cases with different combinations of meteorological input data are investigated to determine the effects of meteorological variables on typhoon prediction. The GAN has

been trained on an NVIDIA Tesla K40c GPU for 72 hours. Table 2 summarizes the considered combinations of the input parameters. Initially, the study attempts 6-h predictions of 10 test typhoons with which the GAN has not been trained. Predictions are connected to a number called a sequence. One sequence stands for $m \times N_i$ chronologically ordered input images that are fed to the GAN, the ground truth data, and the predicted images generated by the network. In the framework of this study, $m = 4$ is applied from a parameter study as the best option [16]. This condition implies that the GAN is fed with information from the past 24 h (4×6 hours).

A. SURFACE VELOCITY

From our previous study [16], it was shown how the addition of surface velocity data to satellite images as inputs to the GAN reduces the average error of typhoon center predictions, how error fluctuations are minimized, and how the quality of predicted cloud images is improved. However, a crucial drawback of the previous study is the reliability of the forecasts. In 5 of 165 test sequences, typhoon centers were not successfully generated by the GAN. This result is unacceptable because blackouts in operational typhoon tracking can have fatal consequences. Therefore, methods to achieve not only accurate but also reliable typhoon forecasts by utilizing both observational and meteorological data are investigated in the subsequent sections.

B. VELOCITY FIELDS AT HIGH ALTITUDES

In Case 1, velocity fields at pressure levels of 200, 850, and 950 mb are added to the inputs in our previous study [16], comprising satellite images and velocity fields at the height of 10 m. These pressure levels are selected due to various reasons. Typhoons are characterized by different maximum speeds at various lateral positions and heights. The eyewall of a typhoon is a ring that surrounds the eye, and it is the most critical area. Measurements of GPS dropwindsonde revealed that hurricanes have their strongest mean eyewall wind speeds at a height of around 500 m [28]. Among the pressure levels from the ERA-interim dataset, the level of 950 mb is the closest to the altitude of 500 m.

Altitudes at pressure levels of 850 and 200 mb are commonly used when analyzing environmental wind shear and its effect on typhoons [29]. In typhoons, wind shear influences the rise of moist air through a column from the surface to high altitudes, where latent heat is released due to condensation. The latent heat supplies a typhoon with energy. Low vertical wind shear strengthens this column and the suction effect inside because the lower and upper parts of the column are aligned. Meanwhile, high vertical wind shear makes it difficult for the column to keep all parts aligned and creates a strong suction effect. Therefore, inputs of Case 1 comprise satellite images, surface velocity, and velocities at pressure levels of 200, 850, and 950 mb.

Predictions for Case 1 show higher reliability than those from the previous study [16] because only one typhoon

center is not identified by the GAN (sequence 21 of typhoon Malakas). In Case 1, the GAN produces a notably high error for sequence 15 of typhoon Neoguri when the typhoon approached the Korean and Japanese mainland (Fig. 2). This peak results in magnified averaged errors and standard deviations for the typhoon Neoguri (Fig. 3). In the images of typhoons Violet and Maemi, the spinning motion is not reproduced clearly (Figs. 4a and c). Saliency maps are analyzed for sequence 15 of TC Maemi (Fig. 5), a challenging sequence with a scattered typhoon close to landfall.

The saliency map of the velocity components is characterized by a high overall score (0.336) that mainly evolves in regions near the typhoon structures (Fig. 5a). This indicates that the instantaneous velocity near such regions plays a major role for track predictions, while it loses its influence with an increased distance from the typhoon center.

C. SURFACE PRESSURE

In Case 2, satellite images are combined with surface pressure data, but without velocity data. Many error peaks are observed, such as in sequence 11 of typhoon Oliwa, sequence 13 of typhoon Maemi, sequence 13 of typhoon Usagi, sequence 6 of typhoon Muifa, and several sequences of typhoon Neoguri before landfall (Fig. 2). One typhoon center is not identified (sequence 16 of typhoon Ramma-sun). Grossly, Cases 2 and 1 show a similar level of reliability, while average errors in Case 2 increase by 40.8% compared to those in Case 1 (Fig. 3). Magnitudes of the average errors in Case 2 are the highest among all cases for all tested typhoons, except for Malakas. Meanwhile, error fluctuations in Case 2 are much higher than that in Case 1 for nearly all tested typhoon (Fig. 3). Specifically, significantly increased uncertainties are observed for typhoons Violet, Oliwa, Maemi, Usagi, Muifa, and Neoguri. The generated images for Case 2 are similar to those in the study of Rüttgers *et al.* [16] (Fig. 4). Clouds appear static, and the spinning motions of cloud structures are not clearly recognized.

In Case 3, data from Case 1 are combined with surface pressure fields. A comparison of results from Cases 1 and 3 indicates that adding surface pressure reduces average errors at all sequences by 3.4% compared to that in Case 1 (Fig. 3). Examples of a stabilizing effect are observed for sequence 9 of typhoon Saomai and sequences 13–15 of typhoon Usagi as it takes a northward deflection. However, predictions at close to landfall are challenging for both cases (Fig. 2). For several typhoons (i.e., Violet, Oliwa, and Maemi), Case 1 shows difficulties when the typhoons approach the mainland. For the other typhoons (i.e., Ramma-sun, Usagi, Muifa, and Malakas), the results in Case 3 show high errors in the same regime. Both cases struggle with the landfall of typhoon Neoguri. The GAN did not reliably predict the center for sequence 10 of typhoon Violet. Overall, cloud images in Case 3 are similar to those in Case 1 (Fig. 4). However, the rotation of typhoon Violet (Fig. 4a) and the dissipating cloud structures below the center of typhoon

TABLE 2. Overview over the input data used in the reference set and the different cases of the parameter study.

Cases	Parameters
Reference set [16]	Satellite image, surface velocity
1	Reference set + velocity at high altitude
2	Reference set - surface velocity + surface pressure
3	Reference set + velocity at high altitude + surface pressure
4	Reference set + velocity at high altitude + surface pressure + sea surface temperature + relative humidity

Maemi (Fig. 4c) are predicted with improved similarity to the ground truth images.

The saliency map of the surface pressure (Fig. 5b) has a lower mean score (0.129) compared to the saliency map of the velocity fields (0.336) (Fig. 5a). This underlines the importance of instantaneous velocity information for the convection-dominated physics of short-term track predictions. However, the interesting aspect we can see in the pressure map is that the global pressure distribution of the complete domain is affecting the path of the typhoon.

D. SEA SURFACE TEMPERATURE AND RELATIVE HUMIDITY

Velocity fields and distribution of surface pressure provide information on the current status of a typhoon. However, the motion and strength depend on physical quantities that affect typhoons with time delay. Sea surface temperature (SST) is such a quantity. In general, warm water on the sea surface ensures high evaporation rates, the high water content in the air, and sufficient energy for typhoons [30]. An SST threshold of around 26.5 °C is typically necessary for strong convection to ensure that enough moist air can rise, and tropical typhoons can form [31]. At temperatures below 26.5 °C, the buoyant force is not strong enough, and sinking overcomes convection. Meanwhile, at an SST above 29.0 °C the convective activity tends to saturate [32]. However, this describes only the interaction between SST and how typhoons develop in the atmosphere. Further, the ocean response to SST should be considered.

Typhoons spin in a cyclonic (counter-clockwise) direction. Their spinning motion couples with the surface layer of the ocean. The scale of a typhoon is large enough to be affected by the Coriolis force of the spinning Earth [33]. This force causes deflection of 90° to the right in the Northern hemisphere. Thus, the surface layer is also deflected, and this phenomenon is known as Ekman transport, which causes upwelling on the ocean surface, where cold water is sucked from the deep ocean [34]. The first reason is that wherever a typhoon moves, cold water is left behind. A second reason is the ocean-upper-layer vertical mixing induced by surface wind friction at the ocean surface. At the surface, breaking waves inject bubbles and generate highly energetic turbulence, leading to an exchange with cooler water from deeper layers [35].

The SST–atmosphere relation and the SST–ocean response can be elaborated with examples from typhoon Maemi. Figs. 6a and b show a satellite image and a corresponding pressure field for a sequence of typhoon Maemi. As shown in

Fig. 6c, in the moving direction of Maemi near the Korean and Japanese coasts, the warm sea surface strengthens the typhoon as it moves northward from its current position [36]. This phenomenon contributed to the disastrous strength of the typhoon near the coast [37]. The cooling effects are visible because SST at the current position of the typhoon is lower than SST in its surroundings.

Another physical quantity that affects typhoons with time delay is relative humidity (RH). Moist environments are associated with large storms once air rises and considerable latent heat is released from condensed water. Furthermore, a large amount of condensed water combined with diverged air at upper levels causes precipitation in outer rainbands. This phenomenon leads to lateral expansion of the typhoon wind field [38]. Meanwhile, dry air limits the strengthening of typhoons. RH is the ratio of the water vapor pressure to the saturated vapor pressure at the equilibrium of a gas–liquid mixture. A percentage value shows the ratio of the current water vapor load to the maximum load of water vapor. The example of typhoon Maemi clearly shows how the typhoon is continuously fed with moist air on its way to the mainland, which is another reason for its high strength (Fig. 6d).

In Case 4, Case 3 data are merged with an SST field and RH fields at pressure levels of 200, 850, and 950 mb. This is the most reliable case because no predictions are omitted by the GAN and is the only case that accurately predicts the centers of the two most challenging typhoons: Usagi and Neoguri (Fig. 2). Unlike other cases, spikes of high errors are not found in the remaining tested typhoons in this case. Except for typhoons Violet and Maemi, adding SST and RH data to Case 3 results in reduced average errors and error fluctuations (Fig. 3). In fact, a reduction of the total average error of 12.9% is achieved in this case. However, the generated images in Case 4 had cloud structures similar to those of Case 3 (Fig. 4). However, predictions appear more reliable because the color intensities of the predicted centers are clearer in all the generated images.

SST and RH had a great influence on the prediction of typhoon tracks, especially when the typhoon is close to land-fall and changes its direction. Errors are mostly reduced in sequences where the typhoon approaches land or afterward. This is underlined by the saliency map of the SST and RH layers (Fig. 5c). Although the overall score (0.142) is in a similar range compared to the pressure map (0.129), local scores do not widely spread over the complete domain. Instead, scores are bundled to the typhoon’s influence area, despite the strong scattering of the storm caused by landfall. This indicates that

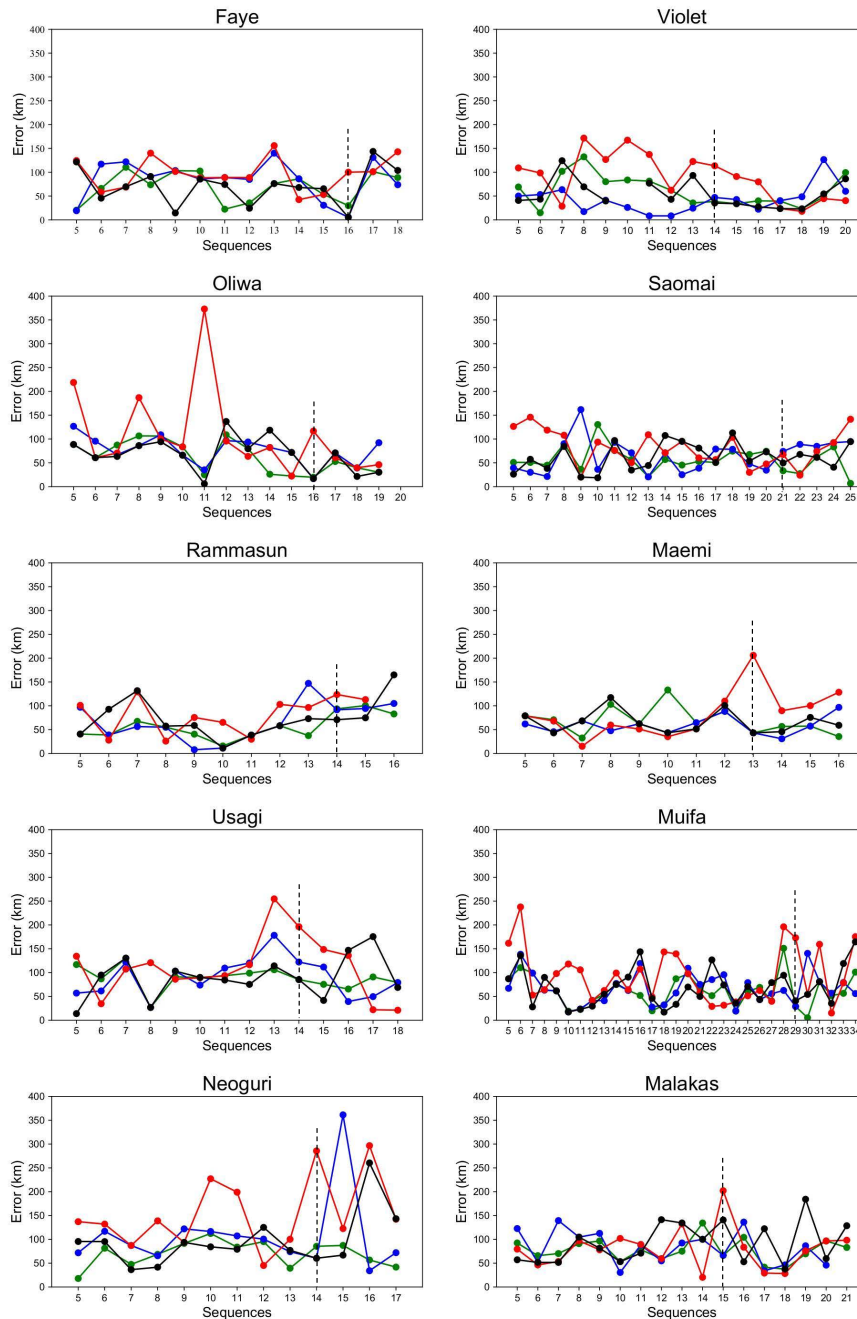


FIGURE 2. Errors between predicted and ground truth typhoon centers measured in kilometers (km). Blue-colored line: Case 1; red-colored line: Case 2; black-colored line: Case 3; green-colored line: Case 4. The sequence of landfall for each typhoon is indicated by the vertical dashed line.

SST and RH are quite helpful in describing the behavior of the typhoon during the typhoon's landing and after. Therefore, in consideration of the improved accuracy and the impact of SST and RH on landfall, the combination in Case 4 is considered as the best option.

IV. EXTENSION FOR 12-H FORECASTS

A. ENLARGEMENT OF THE TYPHOON DATA SET

Predictions in 6-h intervals can help to analyze the effects of different combinations of input data. However, the

application range in a 12-h interval would be much wider to complement established track and intensity forecasting methods in obtaining a faster estimate of sudden changes. The main limitation to such predictions is the number of typhoon data. For the prediction in 12-h intervals, the same number of inputs ($m = 4$) is fed to the GAN for training. However, the GAN predicts information of two future time steps; 6- and 12-h predictions. For this situation, the number of typhoon sequences used to train the GAN in Cases 1–4 is not enough to perform forecasts longer than 6 h. The Korean Meteorological

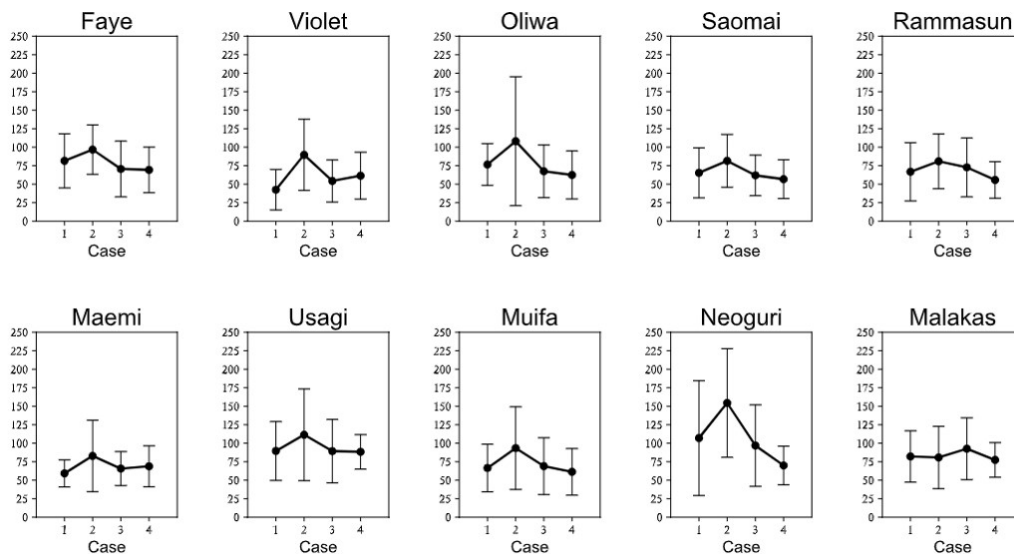


FIGURE 3. Comparison of the average errors measured in kilometers (km) and standard deviations (error bars) for Cases 1–4.

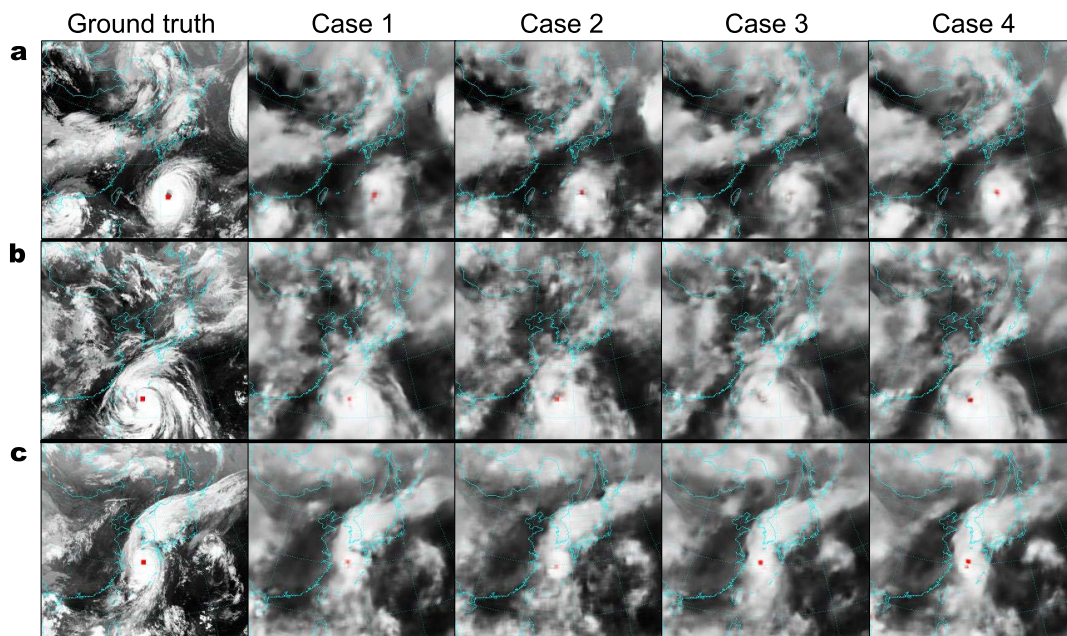


FIGURE 4. Comparisons of the ground truth (satellite) images and the predicted images of typhoon clouds. (a) Sequence 11 of typhoon Violet, (b) sequence 6 of typhoon Rammasun, and (c) sequence 15 of typhoon Maemi.

Agency [18] granted us access to satellite images of only 76 typhoons from 1993 to 2017 that hit or were about to hit the Korean peninsula, from which 66 were used for training and 10 for testing the GAN.

To overcome this limitation, satellite images are replaced with reanalysis data on the total cloud cover (TCC). The TCC achieves a cloud fraction between 0 and 1 by integrating over all cloud layers from the top of the atmosphere down to the surface. A disadvantage of using the TCC data is that rotating

structures of typhoons are not clearly recognizable compared to cloud shapes in satellite images. Hence, vorticity fields at pressure levels of 200, 850, and 950 mb are added to the TCC data to provide information regarding the rotational motions of clouds.

Using reanalysis data rather than satellite images leads to an increase in data from 76 to 757 typhoons. For 20 test cases, a 23.5% reduction on the total average error to 44.5 km (Table 3) in 6-h intervals is achieved.

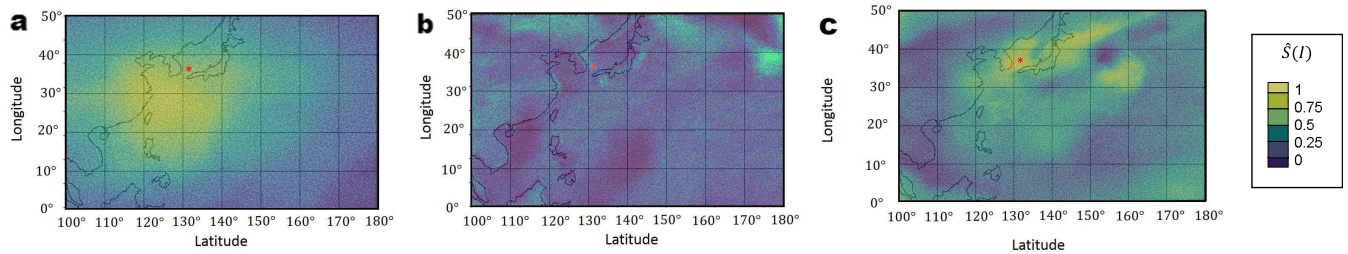


FIGURE 5. Saliency maps with normalized scores $\hat{S}(I)$ for sequence 15 of typhoon Maemi. (a) A saliency map of velocity components at high altitudes, (b) a saliency map of surface pressure, and (c) a saliency map of SST and RH. The red star indicates the center of the typhoon.

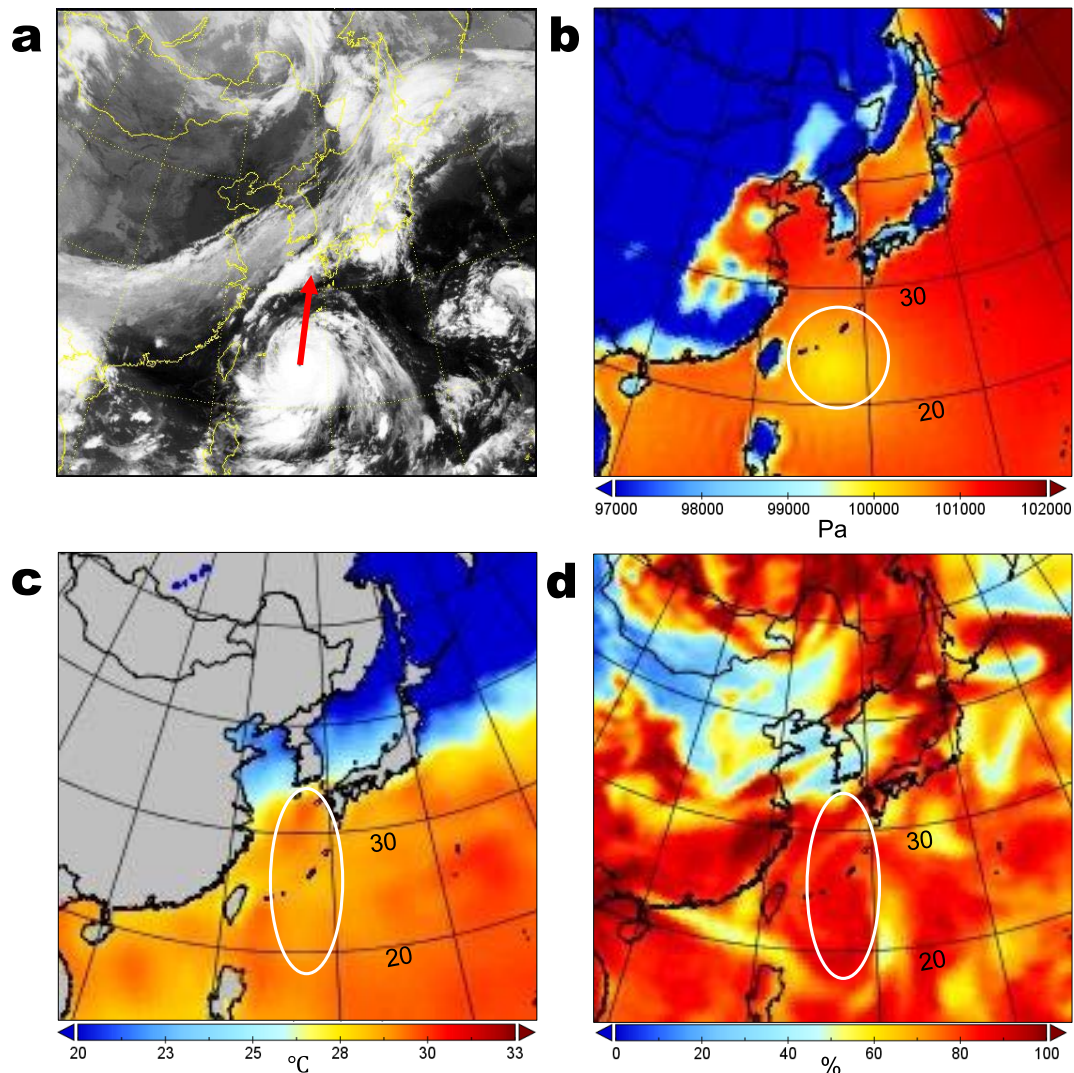


FIGURE 6. Typhoon Maemi on September 10, 2003, at 0:00 Coordinated Universal Time (UTC). (a) Satellite image and moving direction of the typhoon (red arrow), (b) surface pressure (SP) field and low pressure area at the current location of the typhoon (white circle), (c) sea surface temperature (SST) field showing warmer SST in the moving direction (upper part of white ellipse) and cooler SST at the current position of the typhoon (lower part of white ellipse), and (d) relative humidity (RH) field at the pressure level of 850 mb illustrating high RH in the moving direction of the typhoon (upper part of white ellipse), compared to the surrounding area.

B. 6-H AND 12-H FORECASTS OF TYPHOON TRACKS

For Case 4, the red marks for the typhoon centers are visible. However, 12-h time intervals are a challenge to the neu-

ral network and the red marks in the predicted TCC fields frequently become unclear or vanish. To improve predictions, an input channel which contains additional information

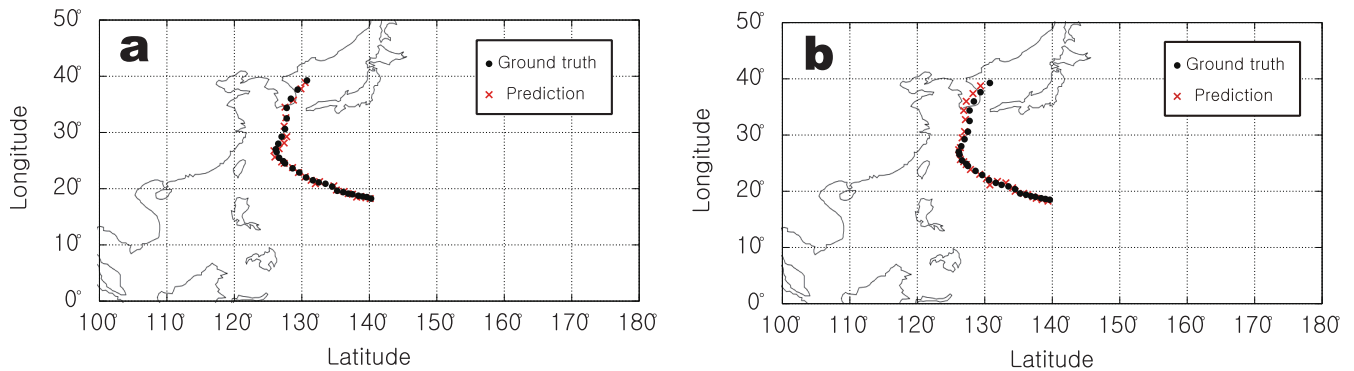


FIGURE 7. Predicted trajectories for typhoon Faye in (a) 6-h interval forecast, and (b) 12-h interval forecast.

about the typhoon center coordinates is added, as explained in Sec. II-B.

In 12-h forecasts, the training data of 737 typhoons and test data of 20 typhoons are used. The 20 test cases are selected with a maximum wind speed of at least 64 knots among over 10 sequences, indicating that typhoons lasted over 60 h. Nine super typhoons that had wind speeds of at least 100 knots classified by the Hong Kong Observatory are also included. Stronger typhoons are more difficult to predict and are selected to test the network performance in extreme conditions. Results of 6- and 12-h forecasts have average errors of 44.5 and 68.7 km, respectively (Table 3). For both intervals, considering only super-typhoons yields increases in the averaged errors by 7.9% and 13.6%, respectively, compared to predictions without super-typhoons. Table 3 presents the detailed results at each time interval for the tested typhoons.

Errors mostly occur when a typhoon is between 120–140 E and 30–50 N. This area is strongly influenced by anti-trade winds such that a typhoon often changes its direction and accelerates northward or eastward [40]. As time intervals increase, errors in typhoon motions near anti-trade winds increase considerably. As an example, the predicted trajectories of typhoon Faye for 6- and 12-h intervals are analyzed as shown in Fig. 7. For 6-h intervals, the predicted centers follow the ground truth with slight errors. For 12-h intervals, the neural network shows difficulties in capturing typhoon motions after sudden deflections.

For typhoons after 1994, the JTWC and the RSMC Tokyo provides forecast data. Table 3 shows a comparison with predictions by the GAN. Since each operational center does not provide data for all typhoons after 1994, predictions of the GAN are partly compared to forecasts of the JTWC, and partly to forecasts of the RSMC Tokyo. For the computation of the average errors of the 12-h comparison only those typhoons are included that have been forecasted by the JTWC or the RSMC Tokyo.

The accuracy of the neural network (66.5 km) has an advantage of 21.6% compared to that of the forecast centers (84.8 km). This trend is observed for predictions without

super-typhoons, as well as for predictions that only contain super-typhoons. Note that trajectories of typhoons and cloud distributions are predicted in less than a second using a single GPU in the present method.

C. 6-H AND 12-H FORECASTS OF TYPHOON INTENSITY

Typhoon intensity is classified by the maximum sustained wind (MSW), which is the speed of surface wind averaged over the past 10 min [39]. The classes are as follows: tropical depression (MSW of 33 knots or fewer), tropical storm (MSW between 34 and 47 knots), severe tropical storm (MSW between 48 and 63 knots), and typhoon (MSW of 64 knots or more). A stronger class (super-typhoon) with MSW of 100 knots or more is added, as officially classified by the Hong Kong Observatory. The Hong Kong Observatory also uses an averaging period of 10 min for their intensity classification.

To forecast typhoon intensity, only the Case 4 configuration is considered. The MSW is derived from the predicted velocity fields at the height of 10 m and then assigned to the corresponding intensity class. The input data, output data, and loss functions match with those from the track predictions. The maximum velocity is observed within a radius of 500 km from the center of a typhoon. The typhoon intensities extracted in time intervals of 6 and 12 h show hit rates of 87.3 and 83.2%, respectively (Table 3). Meanwhile, the average hit rate of super-typhoons is 3.9% lower than the hit rate for the remaining typhoons for 12-h predictions and 2.3% higher for 6-h predictions. Table 3 presents the detailed results at each time interval for the tested typhoons.

As shown in Fig. 8, the present neural network experiences difficulties in predicting strong intensities over 60 knots just before landfall between 25 and 35 N. This can be explained by the fact that instantaneous wind data dissipated during the prediction and errors are accumulated as prediction progresses.

The comparison for typhoons after 1994 with data from forecast centers includes the same typhoons that have been used for the 12-h comparison of track predictions. Again, some intensity predictions are provided by the JTWC,

TABLE 3. Average errors in the prediction of the typhoon track and hit rates of the prediction of the intensity with time intervals of 6 h and 12 h. Typhoons with * are super-typhoons. For typhoons after 1994, 12-h predictions are compared to predictions from JTWC(**) and RSMC Tokyo(***)

Typhoons	Errors in track predictions				Hit rates of intensity predictions			
	6 h	12 h	12 h comparison		6 h	12 h	12 h comparison	
Betty(1987) *	46.13km	76.45km	-		87.1 %	90.3 %	-	
Dan(1999)	39.92km	70.52km	70.52km	61.16km **	86.9 %	82.6 %	82.6 %	93.4 % **
Faye(1995)	36.22km	63.40km	63.40km	94.45km **	90.0 %	80.0 %	80.0 %	83.3 % **
Forrest(1983) *	49.57km	79.15km	-		83.3 %	83.3 %	-	
Lola(1986) *	41.80km	72.69km	-		87.5 %	87.5 %	-	
Maemi(2003) *	48.86km	70.67km	70.67km	59.26km **	88.0 %	88.0 %	88.0 %	100.0 % **
Man-yi(2001)	45.96km	61.59km	61.59km	59.26km **	84.0 %	72.0 %	72.0 %	77.1 % **
Saola(2005)	48.01km	65.60km	65.60km	92.00km ***	90.2 %	82.9 %	82.9 %	89.5 % ***
Sudal(2004)	68.69km	58.82km	58.82km	55.56km **	90.0 %	77.5 %	77.5 %	73.9 % **
Violet(1996)	32.63km	61.12km	61.12km	111.12km **	93.0 %	88.4 %	88.4 %	95.4 % **
Dolye(1981)	34.35km	68.03km	-		86.4 %	90.9 %	-	
Malakas(2016)	39.96km	60.37km	60.37km	73.00km ***	90.0 %	80.0 %	80.0 %	88.9 % ***
Caitlin(1991)	44.65km	78.87km	-		85.7 %	82.8 %	-	
Ellen(1980) *	49.61km	72.51km	-		84.0 %	80.0 %	-	
Gordon(1989) *	45.90km	62.48km	-		80.0 %	84.0 %	-	
Percy(1990) *	41.52km	65.71km	-		84.0 %	88.0 %	-	
Holly(1984)	46.25km	75.67km	-		90.3 %	83.8 %	-	
Nelson(1985)	35.87km	58.22km	-		93.5 %	80.6 %	-	
Oliwa(1997) *	43.52km	76.93km	76.93km	135.20km **	90.3 %	80.6 %	80.6 %	85.9 % **
Sanba(2012) *	49.65km	75.59km	75.59km	107.00km ***	81.2 %	81.2 %	81.2 %	85.0 % ***
Average for all typhoons	44.5km	68.7km	66.5km	84.8km	87.3 %	83.2 %	81.3 %	86.4 %
Average excluding super-typhoons)	42.9km	63.8km	63.1km	72.6km	88.7 %	82.5 %	80.5 %	86.0 %
Average for super-typhoons	46.3km	72.5km	74.4km	100.5km	85.2 %	84.4 %	83.2 %	90.3 %

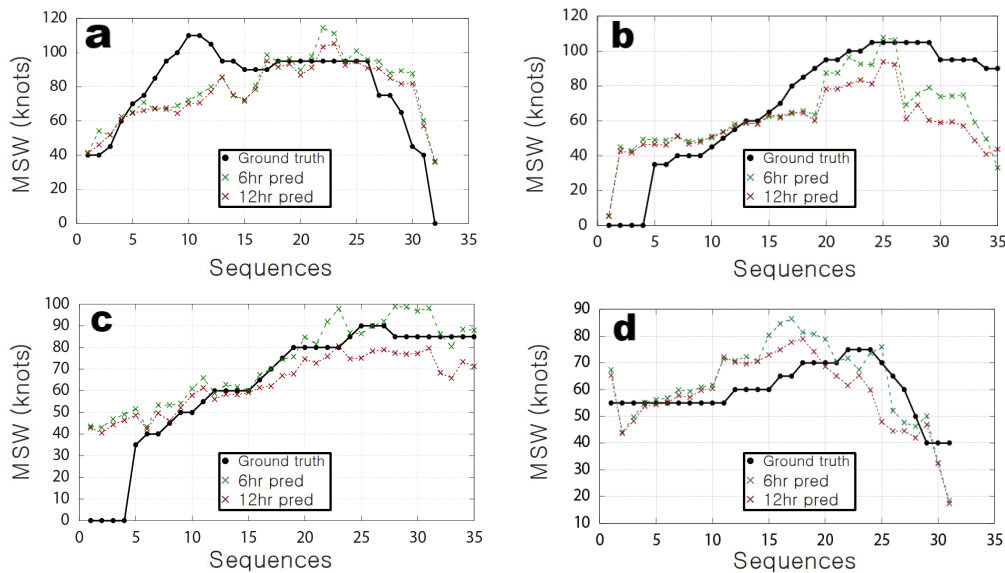


FIGURE 8. Prediction of the intensity of typhoons (a) Faye, (b) Maemi, (c) Sudal, and (d) Betty.

and others by the RSMC Tokyo. For the computation of the average errors of the 12-h comparison only those typhoons are included that have been forecasted by the JTWC or the RSMC Tokyo. Intensity predictions of the GAN yield an average hit rate for all typhoons of 81.3%, compared to 86.4% for forecast centers (Table 3). A similar trend is observed for the averaged hit rates for the case where super-typhoons are excluded. Note that JTWC averages the surface wind over 1 min to classify the typhoon intensity.

V. DISCUSSION

The present method shows a “nowcasting capability” of predicting both the track and intensity of a typhoon within a few seconds using a single GPU. Although the machine-learning-based method is fundamentally different from the typhoon prediction method using numerical simulations, they share important features, especially, dependency on the meteorological variables. Note that the proposed method does not aim to replace the conventional forecasting techniques. It rather shows great potential to complement existing

prediction techniques in yielding faster predictions. The proposed method saves time when starting significant safety measures in case typhoons undergo sudden changes. The present method is expected to be further enhanced by combining a larger amount of observational data with higher-resolution reanalysis data and for longer prediction intervals.

VI. CONCLUSION

In this study, we have developed a GAN-based nowcasting method to predict both the track and intensity of a typhoon up to 12 h. Various combinations of meteorological and observational input data have been investigated to determine which physical parameters favorably influence prediction reliability. Utilization of the velocity fields at different altitudes (200, 850, and 950 mb), surface pressure, sea surface temperature, and relative humidity at different altitudes (200, 850, and 950 mb), total cloud cover, and the vorticity fields at different altitudes (200, 850, and 950 mb) results in the best performance. With these combinations, 6- and 12-h predictions of typhoon tracks and intensities have been conducted.

In typhoon track predictions, the results show average errors of 44.5 and 68.7 km for 6- and 12-h predictions, respectively. Errors mostly occur between 120–140 E and 30–50 N when a typhoon changes the direction and is accelerated. For 12-h intervals, forecasts of operational forecast centers are available for typhoons after 1994 and compared to predictions by the GAN. The present neural network shows an averaged error of 66.5 km in the prediction of typhoon centers, which is more accurate than 84.8 km of the existing typhoon forecast systems for the tested typhoons.

Hit rates of 87.3 and 83.2% are observed for 6- and 12-h interval predictions of the typhoon intensity. The present GAN-based neural network system shows difficulties in predicting high wind speeds over 60 knots, especially before landfall between 25 and 35 N. This can be explained by the dissipation of instantaneous wind data that occurs during prediction and errors accumulated as prediction progressed. For typhoons after 1994, predictions of the typhoon intensity by the GAN (81.3%) and by operational forecast centers (86.4%) show only a small difference of 5.1%.

ACKNOWLEDGMENT

(Mario Rüttgers and Soohwan Jeon contributed equally to this work.) This work was performed as part of the Helmholtz School for Data Science in Life, Earth and Energy (HDS-LEE).

REFERENCES

- [1] C. Schrader. *Hurrikane und Taifune: Wirbelstürme Bewegen Sich Immer Langsamer*. Spiegel. Accessed: Nov. 29, 2021. [Online]. Available: <http://www.spiegel.de/wissenschaft/natur/hurrikane-und-taifune-wirbelstuerme-bewegen-sich-immer-langsamer-a-1211499.html>
- [2] Y. Sun, Z. Zhong, T. Li, L. Yi, Y. Hu, H. Wan, H. Chen, Q. Liao, C. Ma, and Q. Li, "Impact of ocean warming on tropical cyclone size and its destructiveness," *Sci. Rep.*, vol. 7, no. 8154, pp. 1–10, Dec. 2017.
- [3] J. P. Kossin, "A global slowdown of tropical-cyclone translation speed," *Nature*, vol. 558, no. 7708, pp. 104–107, Jun. 2018.
- [4] E. N. Rappaport, J. L. Franklin, L. A. Avila, S. R. Baig, J. L. Beven, II, E. S. Blake, C. A. Burr, J.-G. Jiing, C. A. Juckins, R. D. Knabb, C. W. Landsea, M. Mainelli, M. Mayfield, C. J. McAdie, R. J. Pasch, C. Sisko, S. R. Stewart, and A. N. Tribble, "Advances and challenges at the national hurricane center," *Weather Forecasting*, vol. 24, no. 2, pp. 395–419, Apr. 2009.
- [5] P. Bauer, A. Thorpe, and G. Brunet, "The quiet revolution of numerical weather prediction," *Nature*, vol. 525, no. 7567, pp. 47–55, Sep. 2015.
- [6] *European Centre for Medium Range Weather Forecast (ECMWF)*. Accessed: Nov. 29, 2021. [Online]. Available: <https://www.ecmwf.int/en/about/media-centre/news/2016/what-next-supercomputing-weather-forecasting>
- [7] X. Zhen, Z. Liang, L. Xinzhen, and M. H. Aizhu, "Fast prediction of typhoon tracks based on a similarity method and GIS," *Disaster Adv.*, vol. 6, no. 6, pp. 45–51, 2013.
- [8] M. M. Kordmahalleh, M. G. Sefidmazgi, and A. Homaifar, "A sparse recurrent neural network for trajectory prediction of Atlantic hurricanes," in *Proc. Genetic Evol. Comput. Conf.*, Jul. 2016, pp. 957–964.
- [9] Y. Zhang, R. Chandra, and J. Gao, "Cyclone track prediction with matrix neural networks," in *Proc. Int. Joint Conf. Neural Netw. (IJCNN)*, Jul. 2018, pp. 1–8.
- [10] Z. Chen, X. Yu, G. Chen, and J. Zhou, "Cyclone intensity estimation using multispectral imagery from the FY-4 satellite," in *Proc. Int. Conf. Audio, Lang. Image Process. (ICALIP)*, Jul. 2018, pp. 46–51.
- [11] M. Swarna, N. Sudhakar, and N. Vadaparthi, "An effective tropical cyclone intensity estimation model using convolutional neural networks," *MAUSAM*, vol. 72, no. 2, pp. 281–290, Oct. 2021.
- [12] R. Pradhan, R. S. Aygun, M. Maskey, R. Ramachandran, and D. J. Cecil, "Tropical cyclone intensity estimation using a deep convolutional neural network," *IEEE Trans. Image Process.*, vol. 27, no. 2, pp. 692–702, Feb. 2018.
- [13] M. Alshaye, F. Alawwad, and I. Elshafiey, "Hurricane tracking using Multi-GNSS-R and deep learning," in *Proc. 3rd Int. Conf. Comput. Appl. Inf. Secur. (ICCAIS)*, Mar. 2020, pp. 1–4.
- [14] W. Tian, W. Huang, L. Yi, L. Wu, and C. Wang, "A CNN-based hybrid model for tropical cyclone intensity estimation in meteorological industry," *IEEE Access*, vol. 8, pp. 59158–59168, 2020.
- [15] J. Lian, P. Dong, Y. Zhang, J. Pan, and K. Liu, "A novel data-driven tropical cyclone track prediction model based on CNN and GRU with multi-dimensional feature selection," *IEEE Access*, vol. 8, pp. 97114–97128, 2020.
- [16] M. Rüttgers, S. Lee, S. Jeon, and D. You, "Typhoon track prediction using satellite images in a generative adversarial network," *Scientific Reports*, vol. 9, pp. 1–15, Aug. 2019.
- [17] S. Ravuri, K. Lenc, M. Willson, D. Kangin, R. Lam, P. Mirowski, M. Fitzsimons, M. Athanassiadou, S. Kashem, S. Madge, R. Prudden, A. Mandhane, A. Clark, A. Brock, K. Simonyan, R. Hadsell, N. Robinson, E. Clancy, A. Arribas, and S. Mohamed, "Skillful precipitation nowcasting using deep generative models of radar," *Nature*, vol. 597, pp. 672–677, Jun. 2021.
- [18] Korean Meteorological Administration (KMA). Accessed: Nov. 29, 2021. [Online]. Available: <https://web.kma.go.kr/eng/>
- [19] Japan Meteorological Agency (JMA). Accessed: Nov. 29, 2021. [Online]. Available: <https://www.jma.go.jp/jma/indexe.html>
- [20] *ERA-Interim Public Reanalysis Dataset of the ECMWF*. Accessed: Nov. 29, 2021. [Online]. Available: <http://apps.ecmwf.int/datasets/data/interim-full-daily/levtype=sfc/>
- [21] *European Centre for Medium Range Weather Forecast (ECMWF)*. Accessed: Nov. 29, 2021. [Online]. Available: <https://www.ecmwf.int/>
- [22] D. P. Dee, "The ERA-interim reanalysis: Configuration and performance of the data assimilation system," *Quart. J. Roy. Meteorol. Soc.*, vol. 137, no. 656, pp. 553–597, 2011.
- [23] M. Mathieu, C. Couprie, and Y. LeCun, "Deep multi-scale video prediction beyond mean square error," 2015, *arXiv:1511.05440*.
- [24] C. E. Tilden, "Annual typhoon report," U.S. Fleet Weather Central, Joint Typhoon Warning Center, Honolulu, HI, USA, Tech. Rep., 1959.
- [25] S. Alemany, J. Beltran, A. Perez, and S. Ganzfried, "Predicting hurricane trajectories using a recurrent neural network," 2018, *arXiv:1802.02548*.

- [26] H. Mahmoud and N. Akkari, "Shortest path calculation: A comparative study for location-based recommender system," in *Proc. World Symp. Comput. Appl. Res. (WSCAR)*, Mar. 2016, pp. 1–5.
- [27] K. Simonyan, A. Vedaldi, and A. Zisserman, "Deep inside convolutional networks: Visualising image classification models and saliency maps," 2013, *arXiv:1312.6034*.
- [28] J. L. Franklin, M. L. Black, and K. Valde, "GPS dropwindsonde wind profiles in hurricanes and their operational implications," *Weather Forecasting*, vol. 18, no. 2, pp. 32–44, Mar. 2003.
- [29] S. S. Chen, J. A. Knaff, and F. D. Marks, "Effects of vertical wind shear and storm motion on tropical cyclone rainfall asymmetries deduced from TRMM," *Monthly Weather Rev.*, vol. 134, no. 11, pp. 3190–3208, Nov. 2006.
- [30] H. Ozawa and S. Shimokawa, "Thermodynamics of a tropical cyclone: Generation and dissipation of mechanical energy in a self-driven convection system," *Tellus A, Dyn. Meteorol. Oceanogr.*, vol. 67, no. 1, pp. 1–15, 2015.
- [31] K. J. Tory and R. A. Dare, "Sea surface temperature thresholds for tropical cyclone formation," *J. Climate*, vol. 28, no. 20, pp. 8171–8183, Oct. 2015.
- [32] K.-M. Lau, H.-T. Wu, and S. Bony, "The role of large-scale atmospheric circulation in the relationship between tropical convection and sea surface temperature," *J. Climate*, vol. 10, no. 3, pp. 381–392, Mar. 1997.
- [33] X. Liang and J. C. L. Chan, "The effects of the full coriolis force on the structure and motion of a tropical cyclone. Part I: Effects due to vertical motion," *J. Atmos. Sci.*, vol. 62, no. 10, pp. 3825–3830, Oct. 2005.
- [34] W. Mei, C.-C. Lien, I.-I. Lin, and S.-P. Xie, "Tropical cyclone-induced ocean response: A comparative study of the south China sea and tropical northwest Pacific," *J. Climate*, vol. 28, no. 15, pp. 5952–5968, Aug. 2015.
- [35] J. N. Moum and W. D. Smyth, "Upper ocean mixing processes," in *Encyclopedia of Ocean Sciences*. Amsterdam, The Netherlands: Elsevier, 2001.
- [36] I.-I. Lin, C.-C. Wu, K. A. Emanuel, I.-H. Lee, C.-R. Wu, and I.-F. Pun, "The interaction of supertyphoon maemi (2003) with a warm ocean eddy," *Monthly Weather Rev.*, vol. 133, no. 9, pp. 2635–2649, Sep. 2005.
- [37] K.-S. Yun, J. C. L. Chan, and K.-J. Ha, "Effects of SST magnitude and gradient on typhoon tracks around East Asia: A case study for Typhoon Maemi (2003)," *Atmos. Res.*, vols. 109–110, pp. 36–51, Jun. 2012.
- [38] K. A. Hill and G. M. Lackmann, "Influence of environmental humidity on tropical cyclone size," *Monthly Weather Rev.*, vol. 137, no. 10, pp. 3294–3315, Oct. 2009.
- [39] S. Yoshida, M. Sakai, A. Shouji, M. Hirohata, and A. Shimizu, "Estimation of tropical cyclone intensity using Aqua/AMSR-E data," *Jpn. Meteorol. Agency, Tokyo, Tech. Rep.* 13, 2011.
- [40] L. Wu, Z. Li, J. Duan, and H. Zong, "Sudden tropical cyclone track changes over the western North Pacific: A composite study," *Monthly Weather Rev.*, vol. 141, no. 8, 2013, pp. 2597–2610.
- [41] M. Ranzato, A. Szlam, J. Bruna, M. Mathieu, R. Collobert, and S. Chopra, "Video (language) modeling: A baseline for generative models of natural videos," 2014, *arXiv:1412.6604*.
- [42] D. P. Kingma and J. Ba, "Adam: A method for stochastic optimization," 2014, *arXiv:1412.6980*.



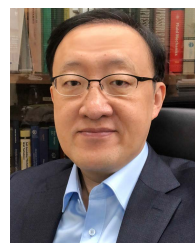
MARIO RÜTTGERS was born in Simmerath, Germany, in 1985. He received the B.S. degree in mechanical engineering from RWTH Aachen University, in 2015, and the M.S. degree in mechanical engineering from the Pohang University of Science and Technology (POSTECH), in 2019. He is currently pursuing the Ph.D. degree with RWTH Aachen University. He attended full-time Korean language courses at Chonnam National University (CNU), Gwangju, South Korea, from 2015 to 2017. Since 2019, he has been working as a Researcher at the Institute of Aerodynamics and Chair of Fluid Mechanics, RWTH Aachen University, and the Jülich Supercomputing Centre (JSC), Forschungszentrum Jülich. He is also associated with the Helmholtz School for Data Science in Life, Earth and Energy (HDS-LEE). His research interests include combining computational fluid dynamics and machine learning techniques.



SOOHWAN JEON was born in Ulsan, South Korea, in 1989. He received the B.S. degree in mechanical engineering from Inha University, in 2015. Since 2015, he has been working as a Researcher at the POSTECH.



SANGSEUNG LEE was born in MI, USA, in 1992. He received the B.S. and Ph.D. degrees in mechanical engineering from the Pohang University of Science and Technology (POSTECH), in 2015 and 2020, respectively. He worked as a Postdoctoral Researcher at the FLOW Center, KTH Royal Institute of Technology, during 2021–2022. He is currently an Assistant Professor with the Department of Mechanical Engineering, Inha University, South Korea.



DONGHYUN YOU received the M.S. degree in scientific computing and computational mathematics and the Ph.D. degree in mechanical engineering from Stanford University, USA. He is currently a Professor with the Department of Mechanical Engineering, POSTECH, South Korea. His research interests include fluid mechanics, turbulent flow, and machine learning.

...